Chemical control of the Rashba spin splitting size of α-GeTe(111) surface states by adjusting the potential at the topmost atomic layer

Hanyoung Ryu,[1,2,*] Jae-Mo Lihm,[1,2,3,*] Joonil Cha,[1,4,5] Beomyoung Kim,[6,7] Beom Seo Kim,[1,2] Wonshik Kyung,[1,2] Inkyung Song,[1] Yeongkwan Kim,[8] Garam Han,[1,2] Jonathan Denlinger,[7] In Chung,[1,4,5] Cheol-Hwan Park,[1,2,3,†] Seung Ryong Park,[9,‡] and Changyoung Kim[1,2,§]

[1]*Center for Correlated Electron Systems, Institute for Basic Science (IBS), Seoul 08826, Republic of Korea*
[2]*Department of Physics and Astronomy, Seoul National University, Seoul 08826, Republic of Korea*
[3]*Center for Theoretical Physics, Seoul National University, Seoul 08826, Republic of Korea*
[4]*Center for Nanoparicle Research, Institute for Basic Science (IBS), Seoul 08826, Republic of Korea*
[5]*School of Chemical and Biological Engineering and Institute of Chemical Processes, Seoul National University, Seoul 08826, Republic of Korea*
[6]*Institute of Physics and Applied Physics, Yonsei University, Seoul 03722, Republic of Korea*
[7]*Advanced Light Source, Lawrence Berkeley National Laboratory, Berkeley, California 94720, USA*
[8]*Graduate School of Nanoscience and Technology, Korea Advanced Institute of Science and Technology, Daejeon 34141, Republic of Korea*
[9]*Department of Physics, Incheon National University, Incheon 22012, Republic of Korea*

As control of the Rashba spin splitting size is highly desirable for spintronic devices, intensive studies have been performed to vary the splitting size by, for example, applying an electric field or designing novel heterostructures. However, direct observation of Rashba spin splitting size change via spectroscopic measurements has not been done so far. Here, we report results of angle-resolved photoemission studies on ferroelectric α-GeTe(111). We observe that the Rashba splitting size of α-GeTe(111) surface states is reduced upon dosing with potassium (K) which has a very low electron affinity. Based on density functional theory calculations, we find that the electric potential energy at the topmost atomic layer and the surface potential energy barrier is reduced upon K dosing. This change in the surface potential induces both delocalization of the surface states and reduction of the splitting size. We expect to increase the splitting size by dosing other elements or molecules with high electron affinity.

I. INTRODUCTION

In solid-state physics, spin-orbit coupling (SOC) caused by relativistic effect accompanies many exotic phenomena. The Rashba effect is one such phenomenon, which has been extensively studied both due to its importance in fundamental science [1–5] and because of its potential for new application platforms in spintronics [6,7]. The Rashba effect has been observed experimentally in various systems, e.g., the surface of solids [8–12], heterostructure interfaces [13], and bulk states of BiTeX (X = I, Br, or Cl) [14–16]. Although these systems show notably large spin splitting, the absence of controllability of the magnitude and chirality of the spin is still a challenge.

Recently, the ferroelectric Rashba semiconductor (FERSC) represented by germanium telluride (GeTe) has attracted attention as an electrically controllable Rashba system [17]. α-GeTe, one of the simplest ferroelectric (FE) semiconductor systems with only two atoms per primitive cell, has bulk Rashba states that are coupled to its FE polarization state. The bulk Rashba states in this material arise from inversion symmetry breaking (ISB) due to intrinsic FE polarization along the (111) direction [17–19]. After the band structure and the possibility of spin control were theoretically predicted [17], the band dispersion, and the controllability of the spin angular momentum (SAM) in the Rashba splitting band in bulk states were studied by angle-resolved photoemission spectroscopy (ARPES) in epitaxially grown GeTe film [20–23]. The (111) surface of GeTe also exhibits Rashba surface states with a sizable spin splitting [20,22,24]. Despite the aforementioned previous theoretical and experimental investigations on GeTe, the microscopic origin and potential controllability of surface Rashba states are yet to be understood comprehensively.

Control of Rashba states such as the control of splitting size and the Rashba coefficient is possible by applying a gate voltage or fabricating a heterostructure [25–27]. The experimental evidence for these methods has mostly been gained from measurements of electronic transport properties [13,28,29]. Direct experimental evidence from spectroscopic methods such as ARPES is desirable. Applying a gate voltage is, however, not

*These authors contributed equally to this work.
†cheolhwan@snu.ac.kr
‡abepark@inu.ac.kr
§changyoung@snu.ac.kr

compatible with ARPES measurements, and observation of interface states is challenging using ARPES. We can mimic applying a gate voltage for ARPES measurements by dosing alkali metal atoms on the surface of the crystal. Because of the low electronegativity of alkali metal atoms, they act as an electron donor when they are absorbed on a crystal. Alkali metal ions with positive charge remain on the crystal surface and affect the electric potential near the surface. As a consequence, the alkali metal provides an effective electric field from the vacuum to the crystal direction [30–32].

In this work, we used high-quality single GeTe crystals to obtain clear band structures and to control the surface Rashba state. We obtained the surface Rashba band for a wide range of k_z dimensions through experimental ARPES measurements with linearly polarized light. The dispersion of the Rashba band was well matched with previous reports, which used the epitaxially grown GeTe films [20,22] and single-crystalline sample [33]. We used *in situ* potassium dosing (K dosing) to systematically control the binding energy and splitting energy of the surface Rashba state and observed a decrease in the Rashba splitting after K dosing. To understand the mechanism behind the experimental results, we performed theoretical calculations based on density functional theory (DFT). The DFT calculations suggested that the delocalization of the surface Rashba state from the crystal surface plays a centrol role in inducing the decrease in the Rashba splitting. We also study the effect of K dosing on the surface SAM and orbital angular momentum (OAM) using DFT calculations.

II. METHODS

All sample preparation processes were conducted in an argon atmosphere (99.99% purity). Pure α-GeTe crystals were synthesized by heating a mixture of elemental Ge and Te (99.999% purity, LTS Research Laboratory, USA) in a 1:1 molar ratio under vacuum ($\sim 10^4$ Torr) in fused-silica tubes at 900 °C for 24 h. The total weight of reactants was 5 g. The powder x-ray diffraction pattern of the ground product matches with the theoretical calculation of rhombohedral α-GeTe phase [Inorganic Crystal Structure Database (ICSD) #159907] [34] without any secondary phase within the detection limit of laboratory XRD. Crystals with a typical dimension larger than ~300 μm size and well-defined faces were manually chosen for the ARPES measurements.

The ARPES experiments were performed at the ARPES end station of beam line 4.0.3 Merlin, Advanced Light Source (ALS), using *p*-polarized photons in the energy range 50–120 eV, and a Scienta R8000 hemisphere analyzer. The angle between the direction of incident photon and the optical axis of the analyzer was 65°. The sample $\bar{K}$-$\bar{\Gamma}$-$\bar{K}$ direction was aligned with the analyzer slit direction. The total energy resolution was set to 18 meV at 90 eV, and the angular resolution was 0.1°, which corresponds to a momentum resolution of 0.004 Å^{-1}. We cleaved the GeTe sample *in situ* to obtain clean surfaces. Experiments were performed at 80 K under a base pressure of less than 6.5×10^{-11} Torr. The *in situ* K-dosing position was the same as the measurement position. During the K dosing, pressure did not exceed 1.5×10^{-10} Torr to protect the sample surface.

We used the QUANTUM ESPRESSO package to perform plane-wave pseudopotential DFT calculations [35]. We used a kinetic energy cutoff of 80 Ry, fully relativistic ONCV pseudopotentials [36] taken from the PseudoDojo library (v0.4) [37], and the PBE functional [38]. The bulk lattice structure was optimized until the internal stress and forces were below 0.01 kbar and 10^{-6} Ry/bohrs, respectively. The optimized hexagonal lattice parameters were $a = 4.233$ Å and $c = 10.921$ Å, which are slightly overestimated compared to experimental values of $a = 4.158$ Å and $c = 10.669$ Å [22]. The Rashba splittings calculated using the relaxed structure and the experimental structure showed a relative difference of at most 10%. For the bulk and slab calculations, $12 \times 12 \times 12$ and $11 \times 11 \times 1$ unshifted k-point grids were used, respectively. For the slab calculation, a 0.015-Ry cold smearing [39] was used to deal with the metallic surface states. In the postprocessing step, we used the projwfc.x program of the QUANTUM ESPRESSO package [35] to project the Kohn-Sham wave functions to the atomic orbitals.

A slab model of GeTe with 31 atomic layers and a 27-Å-thick vacuum was used to compute the surface state electronic structures. We constructed a slab with a Te-terminated surface which terminates after a shorter Te-Ge bond (note that because GeTe is a ferroelectric material there are shorter and longer bonds). We optimized the z coordinates of the topmost six atoms until the forces along the z direction were below 10^{-6} Ry/bohrs while fixing all of the other atoms. The dipole correction was always applied to cancel the unphysical electric field arising from the periodic repetition of slabs with nonzero dipole moments [40].

III. RESULTS AND DISCUSSION

A. Observation of the surface Rasha band changes by K dosing

The crystal structure of GeTe is shown in Fig. 1(a). Above the FE transition temperature $T_c = 720$ K, GeTe has a highly symmetric rock-salt cubic structure (space group $F3m$ No. 225) and is in a paraelectric state. Below T_c, the structure changes to a slightly distorted rhombohedral structure [Fig. 1(a), space group $R3m$ No. 160] [18,19]. The noncentrosymmetric ferroelectricity arises due to the off centering of the Ge (purple) atom along the (111) axis [41]. For a Te-terminated surface of GeTe, the Ge atoms in the second layer are pulled toward the topmost Te layer and those in the fourth layer (Ge) are pulled close to the third layer (Te). Consequently, the Te-terminated surface displays an outward polarization [42]. This FE polarization from the ISB in the bulk atomic configuration induces a large bulk Rashba band splitting at the Z point [17,22]. Figure 1(b) shows the three-dimensional (3D) Brillouin zone (BZ) along with the projected two-dimensional (2D) BZ in the (111) direction. Figure 1(c) displays the Fermi surface (left panel) and the $\bar{M}$-$\bar{\Gamma}$-$\bar{K}$ cut data (right panel) measured using 90-eV photons. The Fermi surface shows clear warped hexagonal surface bands with enhanced Rashba splitting along the $\bar{\Gamma}$-$\bar{K}$ direction compared to the $\bar{\Gamma}$-$\bar{M}$ direction [17,20]. The $\bar{\Gamma}$-$\bar{K}$ and $\bar{\Gamma}$-$\bar{M}$ directions in our experiment and calculation results shown hereafter are the directions parallel with the k_y and k_x axis,

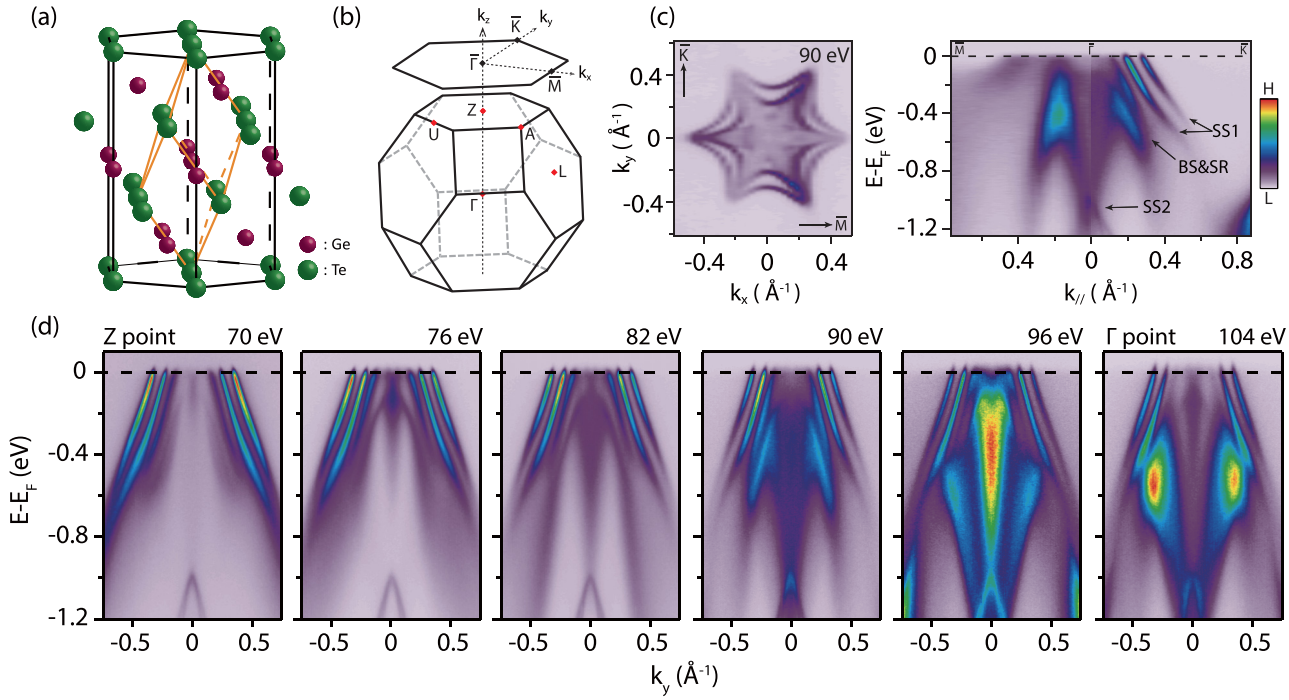

FIG. 1. (a) Crystal structure of GeTe. (b) 3D and [111] direction projected 2D BZ with high-symmetry points. (c) Fermi surface and $\bar{M}$-$\bar{\Gamma}$-$\bar{K}$ high-symmetry cut taken with 90-eV photons. (d) k_z (photon energy) dependent ARPES data along the $\bar{K}$-$\bar{\Gamma}$-$\bar{K}$ direction.

respectively, as presented in Fig. 1(c). We note that the electronic structure of the GeTe(111) surface is sixfold symmetric due to the combination of the threefold rotation and time-reversal symmetries.

To understand the origins of the bands, the $\bar{K}$-$\bar{\Gamma}$-$\bar{K}$ cut data with various photon energies ranging from 50 to 120 eV were taken. Analyzing the k_z-dependent data, we found that the 70- and 104-eV photons probed the Z and Γ points, respectively, with a deduced inner potential value of 14.2 eV, which is comparable to the previous report [20] (please see Fig. 6 for the photon energy-dependent ARPES data and detailed analysis). The $\bar{K}$-$\bar{\Gamma}$-$\bar{K}$ data measured with 70- (Z point) – 104- (Γ point) eV photons are shown in Fig. 1(d). The overall band structure is consistent with the previously reported band structures of the Te-terminated surface [20,22,23], which is energetically more stable than the Ge-terminated surface [43]. Our results exhibit two pairs of sharp surface state bands at different binding energies. In Fig. 1(c), one Rashba pair of surface states crossing the Fermi level is denoted as SS1 and the other surface Rashba pair whose Kramers point is located at around -1 eV is denoted as SS2. Their surface state nature is confirmed by the observation that these states have no k_z dependence. In addition to the surface states, we can observe the bands showing k_z dependence. While the surface states are localized near the surface and exist within the bulk gap without hybridization with the bulk state, the bulk state [BS in Fig. 1(c)] and surface resonance state [SR in Fig. 1(c)] have a longer decay length than the surface states [22].

We attempted to control the surface Rashba states of α-GeTe(111), instead of the bulk Rashba states, by *in situ* K dosing. This method has already been applied to various systems [24,30–32]. We selectively investigated the surface states by taking the data in the second BZ, for which the emission angle in combination with the short photoelectron mean-free path makes ARPES more sensitive to the surface states. We chose 90-eV photon energy at which the bulk states are well separated from the surface states. In the $\bar{K}$-$\bar{\Gamma}$-$\bar{K}$ data in Fig. 2(a), compared to our data shown in Fig. 1(d), we indeed see that surface states stand out more clearly with comparably suppressed intensity from bulk state and surface resonance state. As the K-dosing time increased, we found that the surface state bands monotonically shift to the higher binding energy side accompanied by a decrement in the splitting size between the inner and outer surface Rashba branches. Also seen in the plot is a new feature at the $\bar{\Gamma}$ point that was initially unoccupied but was shifted down below the Fermi energy upon electron doping [24].

To see the changes in surface Rashba splitting more clearly, the momentum distribution curves (MDCs) for various K-dosing time are compared in Fig. 2(b). We used MDCs at the energy that gives the outer band position at $k = 0.31$ Å^{-1}, which is the Fermi momentum of the undoped sample. The blue vertical dashed line marks this wave vector ($k = 0.31$ Å^{-1}). A monotonic decrease in the momentum difference between the two bands was observed upon increasing K-dosing time, from $\Delta k = 0.1$ Å^{-1} before dosing to approximately 0.07 Å^{-1} for dosing time of 300 s. Because the dosing time does not provide an accurate measure of the amount of K dosing, we instead used the binding energy shift as a measure of the amount of K dosing and electron doping. Figure 2(c) shows the band splitting size estimated at $k = 0.31$ Å^{-1} as a function of the binding energy shift. We obtain the binding energies of the outer and inner branches from Lorentzian fit of

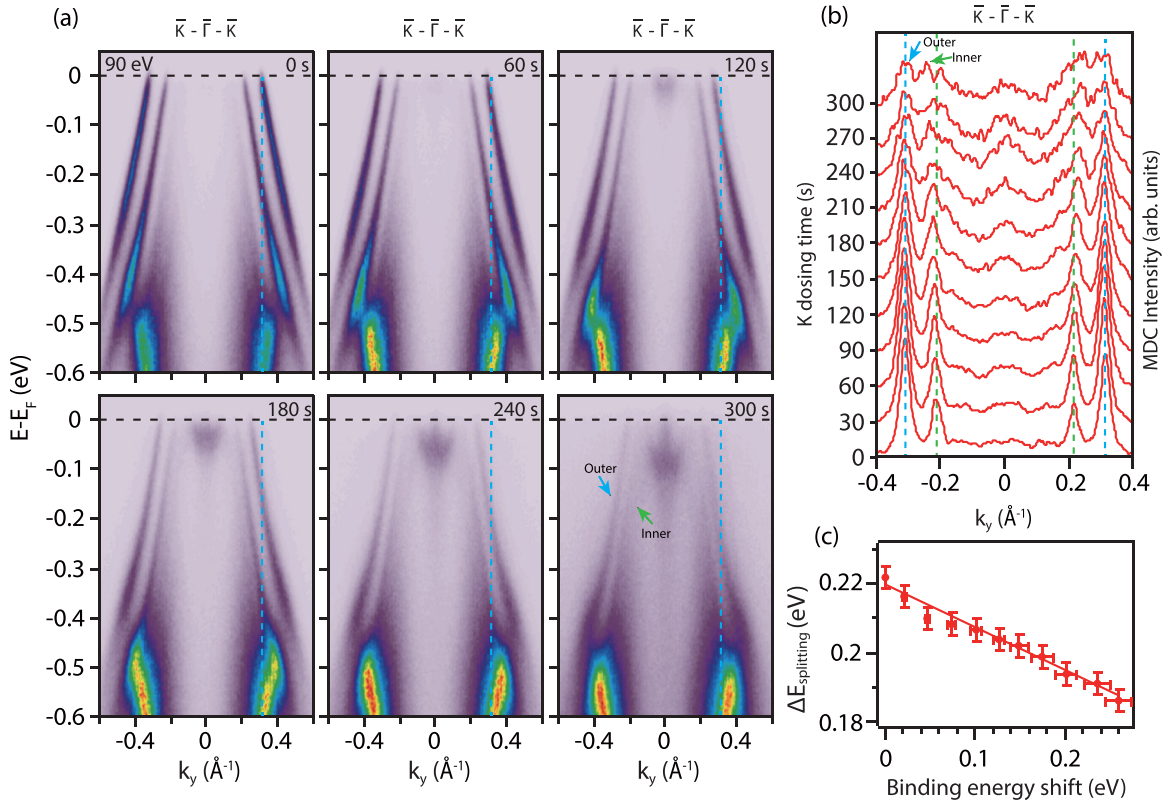

FIG. 2. (a) $\bar{K}$-$\bar{\Gamma}$-$\bar{K}$ cut data for various K-dosing time. The blue vertical dashed line indicates 0.31 Å^{-1}. (b) Momentum distribution curves at the binding energy where the momentum of the outer branch is 0.31 Å^{-1}. The blue (green) vertical dashed line marks the Fermi momentum of the outer (inner) branch of the fresh surface before K dosing. (c) Band splitting size as a function of the binding energy shift.

the energy distribution curves (EDCs). We define the binding energy shift as the change in the average binding energy of the outer and inner branches at $k = 0.31$ Å^{-1}. The splitting size decreases linearly with the amount of the binding energy shift. The splitting energy at the outer branch momentum of $k = 0.31$ Å^{-1} is reduced by about 16% after 300 s of K dosing. A similar study concluded that there was no change in the surface Rashba splitting size after K dosing on GeTe [24]. However, in that work, the ARPES data were taken only with a single 0.09 K-monolayer-doped sample, corresponding to a 0.08-eV binding energy shift. ARPES data at continuously varying K concentrations were not provided. As shown in Fig. 2(c), in our experiments, we clearly observe a continuous Rashba splitting size variation up to a binding energy shift of about 0.25 eV, at which the Rashba splitting is reduced by 16%. We speculate that the 0.09 K monolayer is not enough to clearly distinguish the change in the surface Rashba splitting size [24].

To simulate the effects of K dosing on the surface electronic structure of GeTe, we used a model where a K adatom is placed on top of the relaxed side of the slab. Using an in-plane supercell to change the concentration of the K atom is computationally demanding. Instead, one K atom was placed for each in-plane unit cell and the distance between the adatom and the surface of the slab was tuned to mimic the change in the amount of K dosing [44,45]. This method was proven successful in modeling the effects of K adatoms on the topological surface states of Bi_2Se_3 [45]. The in-plane position of the K adatom was set at that of the topmost Te atom. The structure of the GeTe slab was fixed at the structure optimized without the adatom. The distance between the adatom and the opposite surface of the periodic image of the slab was always kept above 17 Å.

Using this distance-tuning model, we studied the effects of K dosing on the Rashba splitting of the surface states. Figure 3(a) shows the calculated band structure. The surface states on the relaxed surface can be distinguished from other states by inspecting the average depth of the Kohn-Sham wave function. The average depth is defined as $\langle z \rangle_{n\mathbf{k}} = \langle \psi_{n\mathbf{k}} | \hat{z} | \psi_{n\mathbf{k}} \rangle$. A wide range of wave vector where two surface bands close to the Fermi level are linear and parallel can be observed, both along the $\bar{\Gamma}$-$\bar{K}$ and $\bar{\Gamma}$-$\bar{M}$ lines. The band structure is consistent with previous DFT calculations [20,22]. The calculated band structure also coincides with our experimental measurements except for the difference in the Fermi level which can be attributed to the intrinsic Ge vacancy that induces a downward shift of the Fermi level in the experiment [22]. The K adatom band, indicated with blue squares, is well separated from the GeTe surface states at most k points shown in the figure. The bands plotted with solid black lines in Fig. 3(a) are the bulk states or the surface state at the opposite surface of the slab.

For each k point, a pair of surface Rashba states was extracted by picking the two closest-to-surface states within the $[-0.5, 0.5$ eV$]$ window around the Fermi level, using the average depth shown in Fig. 3(a). The difference between

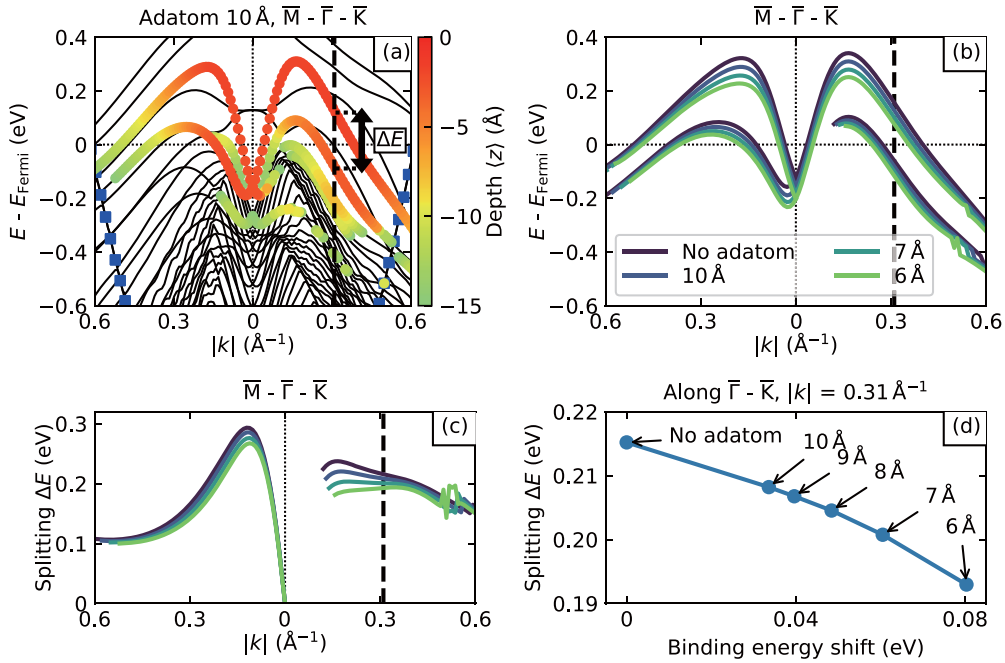

FIG. 3. (a) Band structure of the GeTe slab with a K adatom 10 Å above the slab. The color of disks indicates the average depth of the surface states. The band marked with blue squares is the free-electron-like K adatom band. (b) Band structure of the inner and outer surface states for different K adatom distances. (c) Rashba splitting for different K adatom distances. (d) Rashba splitting at $k_y = 0.31$ Å^{-1} as a function of the binding energy shift. Lines are a guide to the eye. The thick vertical dashed lines in (a)–(c) indicate the k point whose Rashba splitting is plotted in (d).

the energies of the two selected surface Rashba states is the Rashba splitting ΔE. The inner branch of the surface Rashba state was not resolved for the k points on the $\bar{\Gamma}$-$\bar{K}$ line close to $\bar{\Gamma}$ due to the hybridization with other bands. We did not extract the inner surface band in this region.

We note that our calculation, as well as previous DFT calculations [20], fails to reproduce the energy position of Kramers point. Consideration of the p-type doping due to intrinsic Ge vacancies or the use of a semi-infinite surface model might be required to correctly reproduce the energy position of the Kramers point, as done in Refs. [22,24]. Since the calculated Kramers point lies close to the bulk bands, surface states near $\bar{\Gamma}$ along the $\bar{\Gamma}$-$\bar{K}$ direction strongly hybridizes with the bulk bands. Such an effect will be absent in the real system as the Kramers point lies above the Fermi level. Hence, we did not include these states in our analysis of the surface Rashba splitting. In contrast, states far from $\bar{\Gamma}$ with a linear dispersion, which is the major focus of our experiments, suffer less from the error related to the hybridization. Hence, a qualitative comparison between the calculation and experiment is possible.

In Fig. 3(b), we plot the surface state dispersion for different adatom distances [44,45]. We find that the surface bands are shifted downwards and the binding energy increases as the electropositive K adatom moves closer to the slab. Figure 3(c) shows the splitting of the two surface bands. The splitting decreases as the adatom comes closer to the surface, for the entire range of k points plotted, except for $|\mathbf{k}|$ around 0.6 Å^{-1}, where the surface bands are hybridized with the free-electron-like K adatom band. Figure 3(d) shows the computed splitting as a function of the calculated binding energy shift. For the DFT calculations, we defined the binding energy of SS1 as the energy difference between the Kramers point of SS1 and the Fermi level. The binding energy shift is the difference in the binding energy for the slabs with and without K adatoms. The splitting decreases as the binding energy increases. Our DFT calculation using the distance-tuning model qualitatively reproduces our experimental findings shown in Fig. 2(c).

B. Origin of the change in the surface Rashba splitting

To understand why the Rashba splitting decreases after K dosing, we studied the orbital characters of the surface state wave functions, focusing on their weights on each atomic layer. To do so, we projected the Kohn-Shan wave functions to the valence s and p orbitals of the Te and Ge atoms.

The most significant change in the surface state wave functions is the decrease in the weight of the topmost Te atoms. Figures 4(a) and 4(b) show that the surface state weight of the topmost Te atom decreases for all k points as the K adatom is placed closer to the surface. Figure 4(c) shows that the weight of the topmost Te atom is shifted away from the surface towards the inner atoms. We note that the weight of the surface states of the K adatom is below 1% for k points with $|\mathbf{k}| < 0.45$ Å^{-1}.

To understand why the surface states become delocalized, we inspected the Kohn-Sham potential. Figure 4(d) shows the in-plane averaged local potential $V_{\mathrm{avg}}(z)$ near the relaxed surface of the slab. The reference zero of the potentials was shifted so that the potential deep inside the bulk is the same for

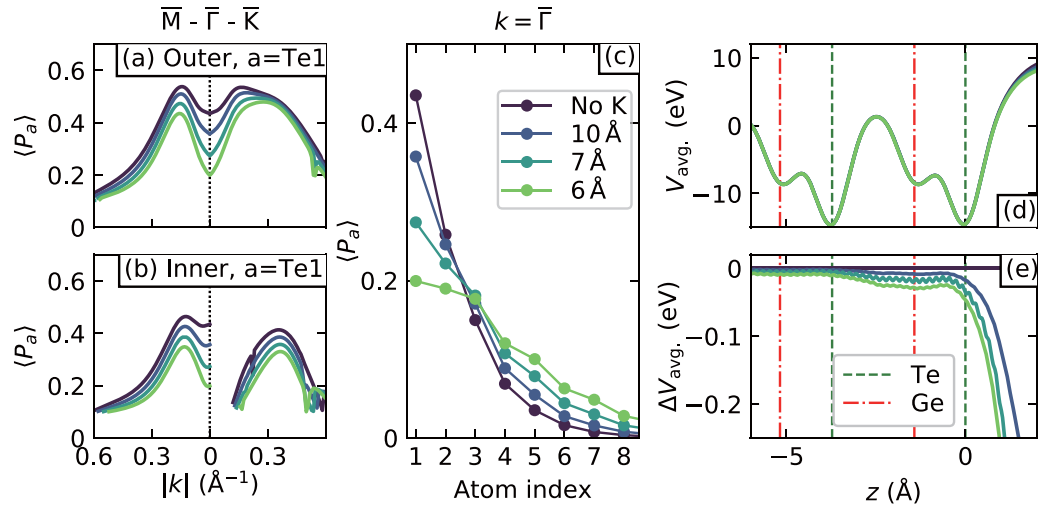

FIG. 4. (a), (b) Projection of the surface state wave functions to the atomic orbitals of the topmost Te (Te1) atom. (c) Layer-resolved projection of the wave function at $k = \bar{\Gamma}$. (d) In-plane averaged local part of the Kohn-Sham potential of the DFT calculation. (e) The difference in the in-plane averaged potential with and without the K adatom. The z coordinate of the topmost Te plane is set to 0.

all slabs. The z coordinate of the topmost Te atoms was set to 0. A steep potential barrier exists near $z = 0$. In Fig. 4(e), we plot the change in $V_{\text{avg}}(z)$ due to the inclusion of the K adatom. As the K adatom is placed closer to the slab, the potential barrier at $z > 0$ softens.

The delocalization of the surface state into the bulk can be understood using first-order perturbation theory for wave functions. When a perturbation $\Delta\hat{V}$ is applied, the first-order change in the weight of the surface state wave function on the topmost Te (Te1) atom is

$$\Delta\langle P_{\text{Te1}}\rangle_{\text{S}} = \sum_{i\neq\text{S}} \frac{\langle\psi_{\text{S}}|\hat{P}_{\text{Te1}}|\psi_i\rangle\langle\psi_i|\Delta\hat{V}|\psi_{\text{S}}\rangle + (\text{c.c.})}{E_{\text{S}} - E_i}. \quad (1)$$

Here, $\hat{P}_{\text{Te1}}$ is the projection operator to the localized atomic orbitals of the topmost Te atom, S indicates the surface state, i is an index for all of the other wave functions at the same k point, and (c.c.) is the complex conjugate of the preceding term. For the surface Rashba states of GeTe, the bulk valence bands and surface resonance bands are close to the surface states in energy position and so will contribute most strongly to $\Delta\langle P_{\text{Te1}}\rangle_{\text{S}}$.

These states are lower in energy than the surface states, i.e., $E_{\text{S}} - E_i > 0$. Next, we simply approximate the functional form of the perturbation as $\Delta\hat{V} \sim -\hat{P}_{\text{Te1}}$. This approximation reflects the fact that as the K adatom approaches the surface, the surface states are shifted downwards in energy [see Fig. 3(b)]. The in-plane average of the potential change shown in Fig. 4(e) also supports this approximation. Then, according to Eq. (1), $\Delta\langle P_{\text{Te1}}\rangle_{\text{S}} < 0$. Thus, the surface state wave function becomes less localized on the topmost Te atom and delocalizes into the bulk.

The decrease in the Rashba splitting is consistent with the Rashba model where the surface electric field couples with the surface electric dipole [46,47]. As shown in Fig. 4(e), the K adatom softens the surface energy barrier, thus reducing the magnitude of the surface electric field. Therefore, the Rashba splitting will decrease as more K atoms are adsorbed. Another factor that one needs to take into account is that the surface state wave function is dispersed among multiple atoms, different from simple monolayer models [48,49]. Hence, the adatom-induced delocalization of the surface state wave functions also affects the Rashba splitting energy.

We expect that the splitting size can be enlarged by dosing other elements or molecules. Due to the low electron affinity of K, the adsorbed K atoms dope electrons to GeTe and become positively charged. This positively charged adatom layer lowers the electric potential barrier at the surface of GeTe, thus reducing the size of the Rashba splitting. By this token, the adsorption of atoms or molecules with a high electron affinity [50–52] will create a negatively charged adatom layer which will enhance the electric potential barrier at the surface. Then, the surface Rashba states will be more localized and have larger spin splitting. To demonstrate this idea, we performed a calculation of a hypothetical situation where a Cl atom, instead of the K atom, is placed above the GeTe(111) surface. Figure 5 shows that the surface potential barrier is hardened and the Rashba splitting indeed increases. We note that we do not expect that Cl atoms can be deposited in an experiment. The suggestion of a specific element or molecule which has a higher electron affinity than GeTe(111) and can be deposited in an actual experiment would require further computational and experimental researches and is beyond the scope of this work. We also suggest that such an effect should be considered to design spintronic device with heterostructure using the surface of interface Rashba states.

It is worthwhile to discuss the role of OAM in the K-dosing-induced Rashba splitting change because OAM is believed as a crucial part of the Rashba band splitting [3,53–57]. By calculating the expectation value of the OAM for the surface Rashba bands, we find that the change in the surface state OAM is dominated by the delocalization of the wave function. The OAM of the topmost Te atom normalized by the wave-function weight on it remains almost unchanged

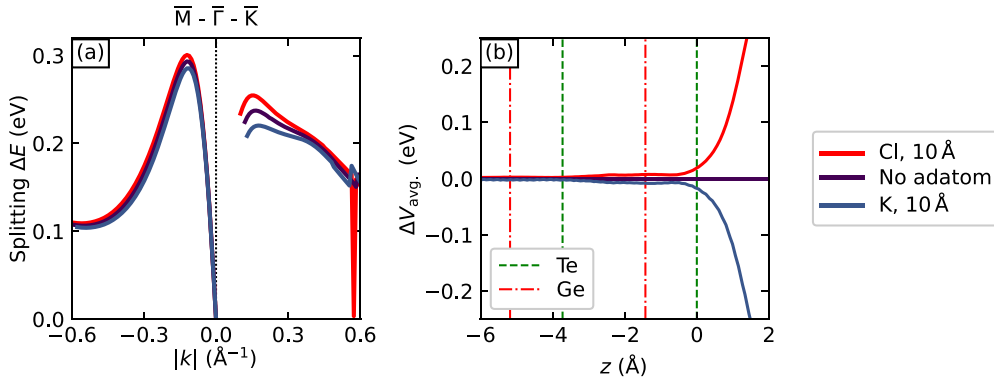

FIG. 5. (a) Surface Rashba splitting for different Cl or K adatom distances. (b) The difference in the in-plane averaged potential with and without the Cl or K adatom.

(see Appendix B, particularly Fig. 11). We believe that the Rashba band splitting itself can be explained by the OAM in GeTe [3,56], but the delocalization of the surface state, rather than the OAM itself, plays a primary role in the reduction of Rashba splitting when K element dosing is applied to the GeTe surface.

IV. SUMMARY

In summary, we have experimentally demonstrated that dosing electropositive K atoms can induce both a downward shift in the overall surface Rashba state and a reduction in the splitting energy. The binding energy shift of the band and the splitting size change exhibited an almost linear relationship. Theoretical analysis based on DFT calculation reveals that the reduction in the Rashba spin splitting size is directly linked to a K-dosing-induced downward shift of the potential energy at the topmost atomic layer. The difference in the weights on the topmost Te atom of the outer and inner band wave functions plays a crucial role, indicating effects beyond the standard two-band picture of the Rashba effect. We expect that the splitting size can be enlarged by dosing other elements or molecules which have high electron affinity. Our results imply the importance of the relative electron affinity between the atomic layer hosting the Rashba states and the adatom. This should be considered in the design of heterostructures utilizing interface Rashba states for spintronic devices [25,58,59].

ACKNOWLEDGMENTS

This work was supported by the Institute for Basic Science in Korea (Grants No. IBS-R009-D1 and No. IBS-R009-G2). J.-M.L. and C.-H.P. were supported by the Creative-Pioneering Research Program through Seoul National University and by the National Research Foundation (NRF) of Korea Grant No. 2020R1A2C1014760. S.R.P. acknowledges support from the NRF (Grant No. 2020R1A2C1011439). The Advanced Light Source is supported by the Office of Basic Energy Sciences of the U.S. DOE under Contract No. DE-AC02-05CH11231. Computational resources have been provided by KISTI (KSC-2019-CRE-0246).

APPENDIX

1. Photon energy (k_z) dependence

ARPES data taken with various photon energies in the range between 50 and 120 eV are shown in Fig. 6. To figure

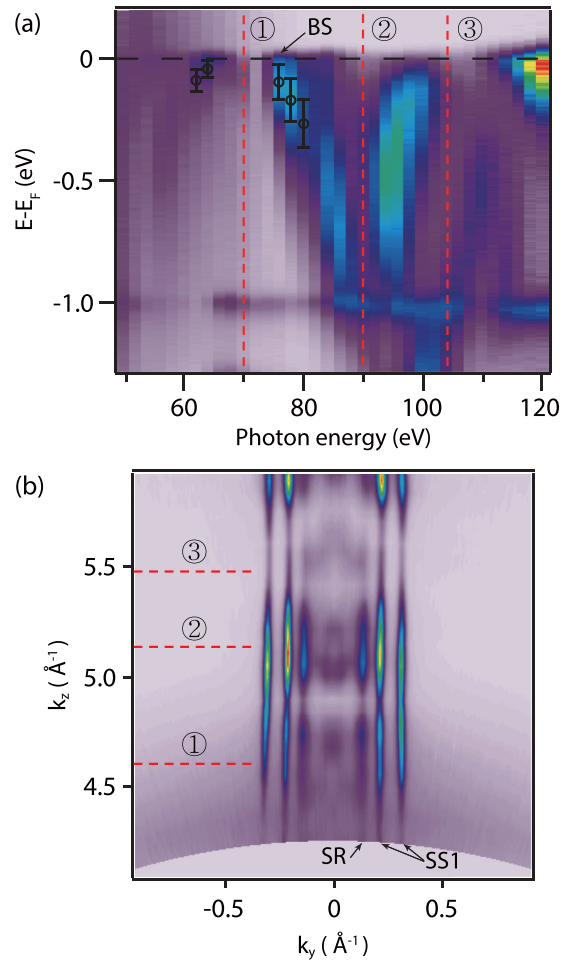

FIG. 6. (a) Photon energy-dependent ARPES data for normal emission. ①, ②, and ③ indicate the spectra measured with 70-, 90-, and 104-eV photon, respectively. (b) k_y-k_z map at the Fermi level taken in the first BZ.

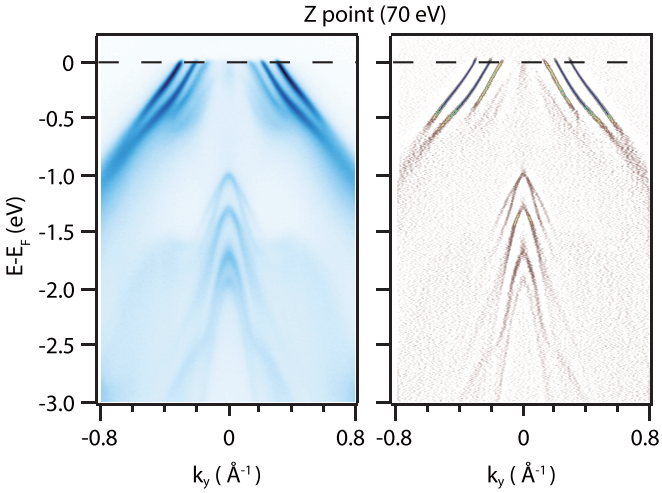

FIG. 7. (Left) $\bar{K}$-$\bar{\Gamma}$-$\bar{K}$ cut data measured with 70-eV photon. (Right) Two-dimensional curvature data of (a).

out the high-symmetry points along the k_z direction, we show a photon energy-dependent ARPES map at $k_x = k_y = 0$ in Fig. 6(a). The Gaussian fitting results of the EDCs of the bulk states are presented with the black circles in Fig. 6(a). Despite the fact that it is not possible to directly observe the Kramers point with (66–74)-eV photon, we can expect that the Kramers point of the bulk states has the maximum kinetic energy in the spectrum measured with 70-eV photon, considering the symmetric dispersion of the bulk states along the k_z axis. Comparing our results with the previous reported k_z-dependent calculation [17] and photon energy-dependent ARPES measurements [20,22], we can conclude that we observed the bulk Z point with 70-eV photon. We deduced the inner potential to be 14.2 eV, taking into account of the lattice constant of α-GeTe [20]. We present a k_y-k_z map at the Fermi level in Fig. 6(b). The bands located at $k_y = 0.31$ and 0.2 Å^{-1} correspond to the outer and inner branch of the SS1, respectively. Because of its 2D nature, SS1 and SR show negligible dispersion along the k_z [23,33].

2. ARPES data near the bulk Z point over a wide energy window

We present ARPES data along the $\bar{K}$-$\bar{\Gamma}$-$\bar{K}$ direction taken with 70-eV photon (Z point) in Fig. 7. It is well known that the bulk Rashba states are not affected by the surface termination except the spin-polarization direction. However, the dispersion of the surface states strongly depends on the surface termination [23]. The overall dispersion shown in Fig. 7 is consistent with previous ARPES and calculation results [20,22,23,33]. This consistency implies that the cleaved surfaces we studied in our ARPES experiments have Te-dominant surface termination and outward polarization.

3. Potassium (K) core-level spectrum

The K 3p core-level spectra with different K-dosing time are shown in Fig. 8(a). We dosed K for up to 420 s and measurements were made at every 30 s. As shown by the red solid line, no K 3p peak was observed from the fresh GeTe surface (0 s) in the binding energy range between 16 and

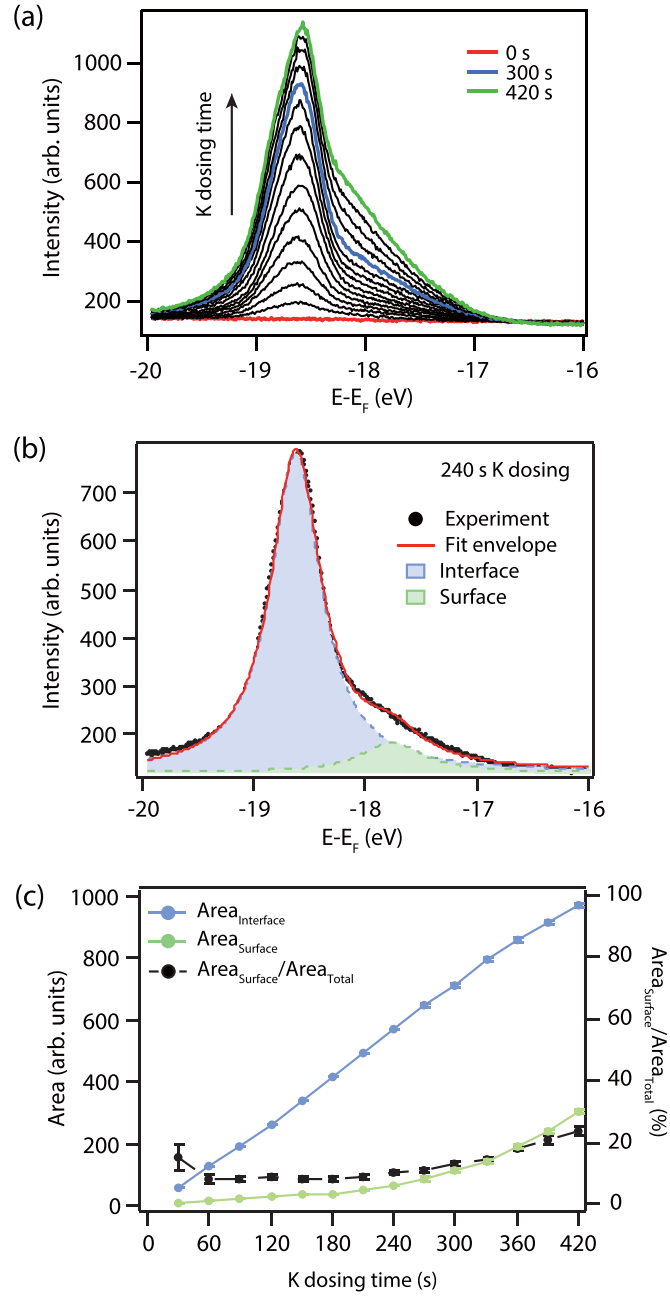

FIG. 8. (a) K 3p core-level spectra for various K-dosing time. The dosing time increases by 30 s for each spectrum. The red, blue, and green solid lines indicate the spectra taken with 0 (fresh surface), 300, and 420 s K dosing, respectively. (b) K 3p core-level spectrum after 240 s K dosing. (c) The peak areas extracted from the spectra in (a) and their ratio as a function of the K-dosing time.

20 eV. The intensity of the K 3p peak shows an asymmetric line shape as shown in 8(a).

To investigate the asymmetric line shape, we performed two Lorentzian fits of the K 3p core-level spectra. In Fig. 8(b), we show the fitting result of 240 s K-dosing data as an example. The fitting result shows two peaks centered at 18.6 and 17.8 eV. The peak area of the 18.6-eV peak (blue shaded) is larger than that of the 17.8-eV peak (green shaded). We

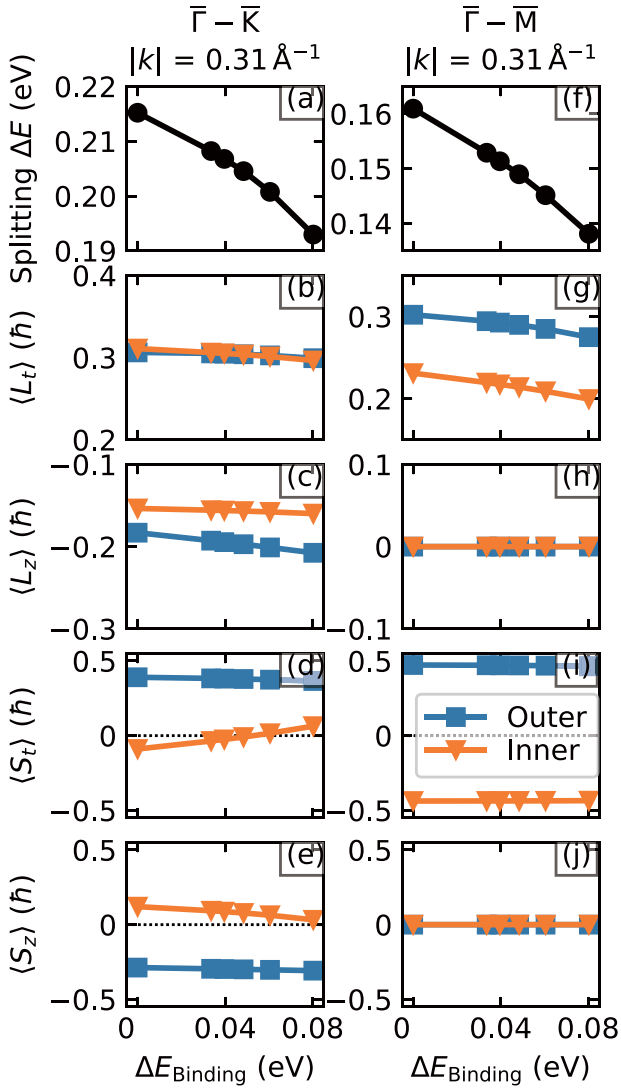

FIG. 9. (a) Rashba splitting, (b) in-plane tangential OAM, (c) out-of-plane OAM, (d) in-plane tangential SAM, and (e) out-of-plane SAM of the surface bands for k points on $\bar{\Gamma}$-$\bar{K}$. (f)–(j) Same quantities as in (a)–(e) for k points on $\bar{\Gamma}$-$\bar{M}$. For the tangential components, positive values indicate clockwise direction.

calculate the ratio between the areas of the two peaks as a function of the K-dosing time up to 420 s. The results are shown in Fig. 8(c). The peak positions and the binding energy difference between the two peaks are similar to the previously reported values [31,60]. The peak at 17.8 eV exists almost before the intensity of the 18.6-eV peak saturates, indicating that the growth mode is not an ideal layer by layer but has some inhomogeneous growth such as island growth.

4. OAM and SAM of surface Rashba state

We study the SAM and OAM of the surface states, which are directly related to the Rashba splitting. Figure 9 shows the tangential and out-of-plane components of the SAM and OAM of the surface states. For states with k points along $\bar{\Gamma}$-$\bar{M}$ and $\bar{\Gamma}$-$\bar{K}$, the radial components are zero due to the mirror and time-reversal symmetries of the lattice. The SAM and OAM along the z axis are also zero on the $\bar{\Gamma}$-$\bar{M}$ line due to the mirror symmetry. From Fig. 9, we note two major changes in the SAM and OAM with increasing binding energy shift ($\Delta E_{\text{binding}}$): (i) the direction of the in-plane SAM of the inner band on the $\bar{\Gamma}$-$\bar{K}$ line smoothly flips from clockwise to counterclockwise [Fig. 9(d)], and (ii) the magnitude of the in-plane OAM of both bands decreases on the $\bar{\Gamma}$-$\bar{M}$ line [Fig. 9(g)].

To understand the change in SAM, we plot the in-plane tangential SAM of the surface states in Figs. 10(a) and 10(b). We find that there are surface resonance states below the inner Rashba states whose in-plane SAM are along the counterclockwise direction. These states are the surface resonance states, which have been found both theoretically and experimentally [20,22]. Because the inner Rashba band and the surface resonance bands are energetically close, they can easily hybridize with each other. As the Rashba surface states become delocalized towards the bulk by the K adatom, the hybridization with the surface resonance states, which have greater weight in the bulk than the surface states, will become stronger. Thus, the SAM of the surface resonance states can be transferred to the inner surface state, leading to the flip of the in-plane SAM. This picture is supported by the fact that the in-plane SAM of the S4 surface resonance band decreases

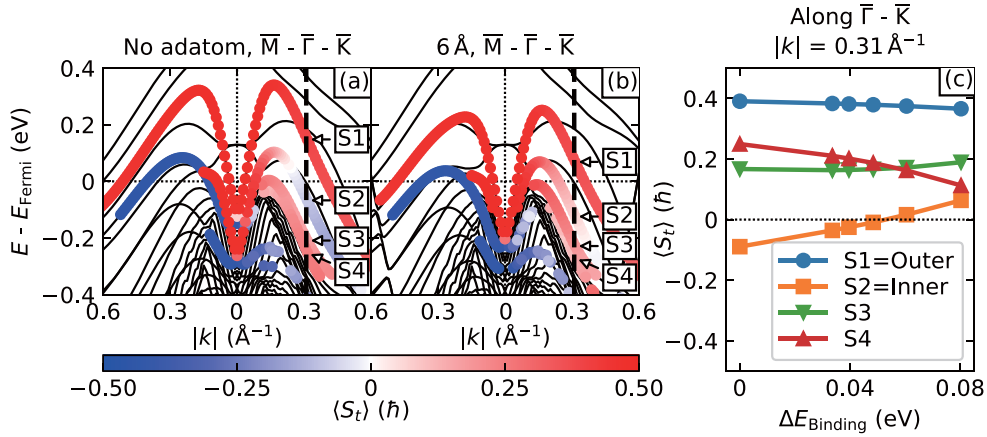

FIG. 10. (a), (b) Band structure and in-plane tangential SAM of the surface states for a slab model (a) without K adatoms, and (b) with K adatoms 6 Å above the slab. (c) In-plane tangential SAM of the four surface and surface resonance states marked in (a) and (b).

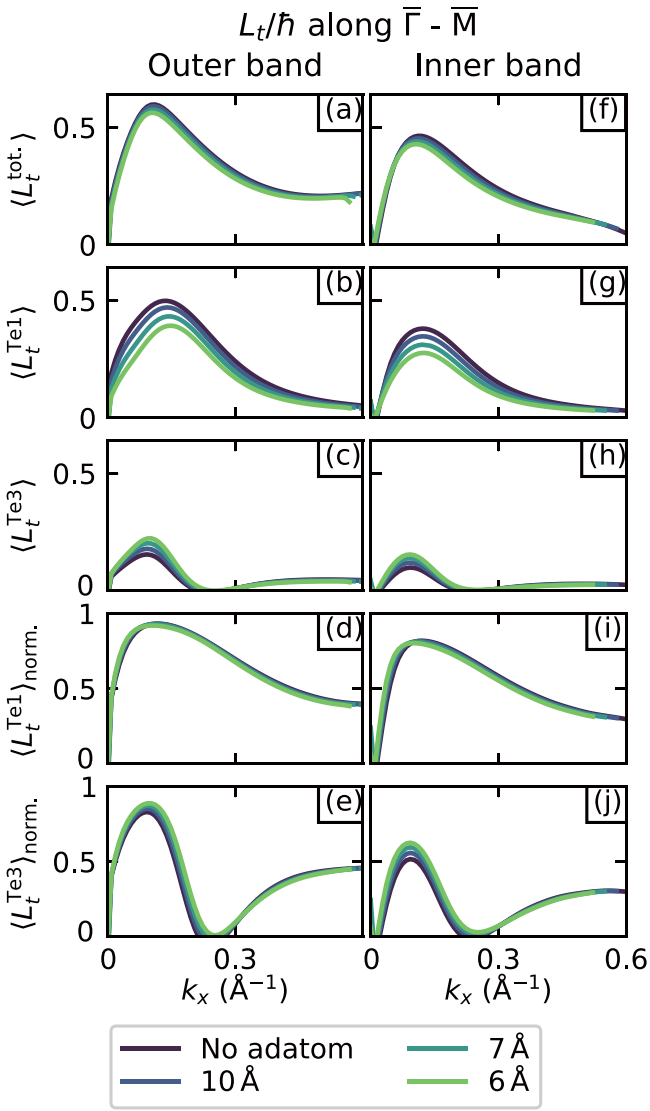

FIG. 11. (a)–(e) In-plane tangential OAM of the outer Rashba band. (a) Total OAM, (b), (c) contribution of the topmost Te layer (Te1) [(b)] and the third layer, which is a Te layer, (Te3) [(c)] to the total OAM, (d), (e) normalized OAM of the Te1 and Te3 layers. (f)–(j) Same plots as in (a)–(e) for the inner Rashba band.

by a similar amount to the increase in the in-plane SAM of the inner Rashba band [Fig. 10(c)].

Now, let us examine the decrease in the OAM on the $\bar{\Gamma}$-$\bar{M}$ line. Hybridization with surface resonance bands cannot be the cause because there are no low-energy surface resonance bands on the $\bar{\Gamma}$-$\bar{M}$ line. To investigate further, we compute the contribution of each atomic layer to the total OAM. The layer-resolved OAM without and with normalization are defined as

$$\langle \vec{L}^a \rangle = \langle \psi_{n\mathbf{k}} | \hat{\vec{L}} \hat{P}_a | \psi_{n\mathbf{k}} \rangle$$

and

$$\langle \vec{L}^a \rangle_{\mathrm{norm}} = \langle \psi_{n\mathbf{k}} | \hat{\vec{L}} \hat{P}_a | \psi_{n\mathbf{k}} \rangle / \langle \psi_{n\mathbf{k}} | \hat{P}_a | \psi_{n\mathbf{k}} \rangle,$$

respectively, where $\hat{\vec{L}}$ is the angular momentum operator and $\hat{P}_a$ is the projection operator to the valence p orbitals of atom a. In Fig. 11, we show the contribution of the topmost and third atomic layers, which are Te layers, to the OAM. The contributions of the other layers including the second layer, which is a Ge layer, are at least four times smaller. From Fig. 11, we find that while the OAM of the topmost Te layer without normalization decreases considerably with K dosing, the normalized OAM does not change appreciably. Hence, the decrease in the OAM of the topmost Te layer occurs because of the decreased weight of the wave function on the topmost Te layer, not because of the decrease in the OAM of the topmost Te atom. Thus, the K-adatom-induced delocalization of the surface states is also responsible for the change in the total OAM. On the $\bar{\Gamma}$-$\bar{M}$ line, the SAM are almost fully polarized at all K adatom distances [Fig. 9(i)]. In addition, the OAM of the two Rashba bands are parallel, while their SAM are antiparallel. This configuration corresponds to the case where the ISB is dominant over the SOC so that the SOC acts perturbatively to generate an effective Zeeman field that splits the oppositely spin-polarized bands [53]. Because the magnitude of the effective Zeeman field is proportional to the OAM, the decrease in the OAM on the $\bar{\Gamma}$-$\bar{M}$ line with increasing binding energy [Fig. 9(g)] will contribute to the reduction of the splitting of the Rashba bands.

[1] G. Dresselhaus, Phys. Rev. **100**, 580 (1955).
[2] Y. A. Bychkov and E. I. Rashba, J. Phys. C: Solid State Phys. **17**, 6039 (1984).
[3] S. R. Park, C. H. Kim, J. Yu, J. H. Han, and C. Kim, Phys. Rev. Lett. **107**, 156803 (2011).
[4] K. Yaji, Y. Ohtsubo, S. Hatta, H. Okuyama, K. Miyamoto, T. Okuda, A. Kimura, H. Namatame, M. Taniguchi, and T. Aruga, Nat. Commun. **1**, 17 (2010).
[5] C. R. Ast, J. Henk, A. Ernst, L. Moreschini, M. C. Falub, D. Pacilé, P. Bruno, K. Kern, and M. Grioni, Phys. Rev. Lett. **98**, 186807 (2007).
[6] I. M. Miron, G. Gaudin, S. Auffret, B. Rodmacq, A. Schuhl, S. Pizzini, J. Vogel, and P. Gambardella, Nat. Mater. **9**, 230 (2010).
[7] I. M. Miron, T. Moore, H. Szambolics, L. D. Buda-Prejbeanu, S. Auffret, B. Rodmacq, S. Pizzini, J. Vogel, M. Bonfim, A. Schuhl, and G. Gaudin, Nat. Mater. **10**, 419 (2011).
[8] S. LaShell, B. A. McDougall, and E. Jensen, Phys. Rev. Lett. **77**, 3419 (1996).
[9] M. Hoesch, M. Muntwiler, V. N. Petrov, M. Hengsberger, L. Patthey, M. Shi, M. Falub, T. Greber, and J. Osterwalder, Phys. Rev. B **69**, 241401(R) (2004).
[10] C. R. Ast and H. Höchst, Phys. Rev. Lett. **87**, 177602 (2001).
[11] Y. M. Koroteev, G. Bihlmayer, J. E. Gayone, E. V. Chulkov, S. Blügel, P. M. Echenique, and Ph. Hofmann, Phys. Rev. Lett. **93**, 046403 (2004).

[12] M. Z. Hasan and C. L. Kane, Rev. Mod. Phys. **82**, 3045 (2010).
[13] J. Nitta, T. Akazaki, H. Takayanagi, and T. Enoki, Phys. Rev. Lett. **78**, 1335 (1997).
[14] K. Ishizaka, M. S. Bahramy, H. Murakawa, M. Sakano, T. Shimojima, T. Sonobe, K. Koizumi, S. Shin, H. Miyahara, A. Kimura, K. Miyamoto, T. Okuda, H. Namatame, M. Taniguchi, R. Arita, N. Nagaosa, K. Kobayashi, Y. Murakami, R. Kumai, Y. Kaneko *et al.*, Nat. Mater. **10**, 521 (2011).
[15] G. Landolt, S. V. Eremeev, O. E. Tereshchenko, S. Muff, B. Slomski, K. A. Kokh, M. Kobayashi, T. Schmitt, V. N. Strocov, and J. Osterwalder, New J. Phys. **15**, 085022 (2013).
[16] A. Crepaldi, L. Moreschini, G. Autés, C. Tournier-Colletta, S. Moser, N. Virk, H. Berger, Ph. Bugnon, Y. J. Chang, K. Kern, A. Bostwick, E. Rotenberg, O. V. Yazyev, and M. Grioni, Phys. Rev. Lett. **109**, 096803 (2012).
[17] D. Di Sante P. Barone R. Bertacco, and S. Picozzi, Adv. Mater. **25**, 509 (2013).
[18] T. Chattopadhyay, J. X. Boucherle, and H. G. vonSchnering, J. Phys. C: Solid State Phys. **20**, 1431 (1987).
[19] K. M. Rabe and J. D. Joannopoulos, Phys. Rev. B **36**, 6631 (1987).
[20] M. Liebmann, C. Rinaldi, D. Di Sante, J. Kellner, C. Pauly, R. N. Wang, J. E. Boschker, A. Giussani, S. Bertoli, M. Cantoni, L. Baldrati, M. Asa, I. Vobornik, G. Panaccione, D. Marchenko, J. Sánchez-Barriga, O. Rader, R. Calarco S. Picozzi, R. Bertacco, and M. Morgenstern, Adv. Mater. **28**, 560 (2016).
[21] H. J. Elmers, R. Wallauer, M. Liebmann, J. Kellner, M. Morgenstern, R. N. Wang, J. E. Boschker, R. Calarco, J. Sánchez-Barriga, O. Rader, D. Kutnyakhov, S. V. Chernov, K. Medjanik, C. Tusche, M. Ellguth, H. Volfova, S. Borek, J. Braun, J. Minár, H. Ebert, and G. Schönhense, Phys. Rev. B **94**, 201403(R) (2016).
[22] J. Krempaský, H. Volfová, S. Muff, N. Pilet, G. Landolt, M. Radović, M. Shi, D. Kriegner, V. Holý, J. Braun, H. Ebert, F. Bisti, V. A. Rogalev, V. N. Strocov, G. Springholz, J. Minár, and J. H. Dil, Phys. Rev. B **94**, 205111 (2016).
[23] C. Rinaldi, S. Varotto, M. Asa, J. Sławińska, J. Fujii, J. Vinai, S. Cecchi, D. Di Sante, R. Calarco, I. Voborbik, G. Panaccione, S. Picozzi, and R. Bertacco, Nano Lett. **18**, 2751 (2018).
[24] G. Kremer, T. Jaouen, B. Salzmann, L. Nicolaï, M. Rumo, C. W. Nicholson, B. Hildebrand, J. H. Dil, J. Minár, G. Springholz, J. Krempaský, and C. Monney, Phys. Rev. Res. **2**, 033115 (2020).
[25] J.-J. Zhou, W. Feng, Y. Zhang, S. A. Yang, and Y. Yao, Sci. Rep. **4**, 3841 (2014).
[26] S.-J. Gong, C.-G. Duan, Y. Zhu, Z.-Q. Zhu, and J.-H. Chu, Phys. Rev. B **87**, 035403 (2013).
[27] L. Xiang, Y. Ke, and Q. Zhang, Appl. Phys. Lett. **115**, 203501 (2019).
[28] K. Premasiri, S. K. Radha, S. Sucharitakul, U. R. Kumar, R. Sankar, F.-C. Chou, Y.-T. Chen, and X. P. A. Gao, Nano Lett. **18**, 4403 (2018).
[29] M. Schultz, F. Heinrichs, U. Merkt, T. Colin, T. Skauli, and S. Løvold, Semicond. Sci. Technol. **11**, 1168 (1996).
[30] T. Ohta, A. Bostwick, T. Seyller, K. Horn, and E. Rotenberg, Science **313**, 951 (2006).
[31] Y. K. Kim, O. Krupin, J. D. Denlinger, A. Bostwick, E. Rotenberg, Q. Zhao, J. F. Mitchell, J. W. Allen, and B. J. Kim, Science **345**, 187 (2014).
[32] J. Kim, S. S. Baik, S. H. Ryu, Y. Sohn, S. Park, B.-G. Park, J. Denlinger, Y. Yi, H. J. Choi, and K. S. Kim, Science **349**, 723 (2015).
[33] A. S. Frolov, J. Sánchez-Barriga, C. Callaert, J. Hadermann, A. V. Fedorov, D. Yu. Usachov, A. N. Chaika, B. C. Walls, K. Zhussupbekov, I. V. Shvets, M. Muntwiler, M. Amati, L. Gregoratti, A. Yu. Varykhalov, O. Rader, and L. V. Yashina, ACS Nano **14**, 16576 (2020).
[34] NIST Inorganic Crystal Structure Database, NIST Standard Reference Database Number 3, National Institute of Standards and Technology,Gaithersburg, M.D. 20899 (National Institute of Standards and Technology, Gaithersburg, MD, USA, 2018), https://doi.org/10.18434/M32147.
[35] P. Giannozzi, S. Baroni, N. Bonini, M. Calandra, R. Car, C. Cavazzoni, D. Ceresoli, G. L. Chiarotti, M. Cococcioni, I. Dabo, A. Dal Corso, S. de Gironcoli, S. Fabris, G. Fratesi, R. Gebauer, U. Gerstmann, C. Gougoussis, A. Kokalj, M. Lazzeri, L. Martin-Samos *et al.*, J. Phys.: Condens. Matter **21**, 395502 (2009).
[36] D. R. Hamann, Phys. Rev. B **88**, 085117 (2013).
[37] M. van Setten, M. Giantomassi, E. Bousquet, M. Verstraete, D. Hamann, X. Gonze, and G.-M. Rignanese, Comput. Phys. Commun **226**, 39 (2018).
[38] J. P. Perdew, K. Burke, and M. Ernzerhof, Phys. Rev. Lett. **77**, 3865 (1996).
[39] N. Marzari, D. Vanderbilt, A. De Vita, and M. C. Payne, Phys. Rev. Lett. **82**, 3296 (1999).
[40] L. Bengtsson, Phys. Rev. B **59**, 12301 (1999).
[41] F. Kadlec, C. Kadlec, P. Kužel, and J. Petzelt, Phys. Rev. B **84**, 205209 (2011).
[42] A. V. Kolobov, D. J. Kim, A. Giussani, P. Fons, J. Tominaga, R. Calarco, and A. Gruverman, APL Mater. **2**, 066101 (2014).
[43] V. L. Deringer, M. Lumeij, and R. Dronskowski, J. Phys. Chem. C **116**, 15801 (2012).
[44] J. W. Villanova, E. Barnes, and K. Park, Nano Lett. **17**, 963 (2017).
[45] K. Park, C. De Beule, and B. Partoens., New J. Phys. **15**, 113031 (2013).
[46] J. Hong, J.-W. Rhim, C. Kim, S. R. Park, and J. H. Shim, Sci. Rep. **5**, 13488 (2015).
[47] B. Kim, P. Kim, W. Jung, Y. Kim, Y. Koh, W. Kyung, J. Park, M. Matsunami, S. I. Kimura, J. S. Kim, J. H. Han, and C. Kim, Phys. Rev. B **88**, 205408 (2013).
[48] L. Petersen and P. Hedegård, Surf. Sci. **459**, 49 (2000).
[49] G. Khalsa, B. Lee, and A. H. MacDonald, Phys. Rev. B **88**, 041302(R) (2013).
[50] S. Y. Zhou, D. A. Siegel, A. V. Fedorov, and A. Lanzara, Phys. Rev. Lett. **101**, 086402 (2008).
[51] D. Hsieh, Y. Xia, D. Qian, L. Wray, J. H. Dil, F. Meier, J. Osterwalder, L. Patthey, J. G. Checkelsky, N. P. Ong, A. V. Fedorov, H. Lin, A. Bansil, D. Grauer, Y. S. Hor, R. J. Cava, and M. Z. Hasan, Nature (London) **460**, 1101 (2009).
[52] N. Liu, C. Ju, X. M. Cheng, and X. S. Miao, J. Electron. Mater. **43**, 3105 (2014).
[53] V. Sunko, H. Rosner, P. Kushwaha, S. Khim, F. Mazzola, L. Bawden, O. J. Clark, J. M. Riley, D. Kasinathan, M. W. Haverkort, T. K. Kim, M. Hoesch, J. Fujii, I. Vobornik, A. P. Mackenzie, and P. D. C. King, Nature (London) **549**, 492 (2017).
[54] L. Ponet and S. Artyukhin, Phys. Rev. B **98**, 174102 (2018).

[55] S. R. Park, J. Han, C. Kim, Y. Y. Koh, C. Kim, H. Lee, H. J. Choi, J. H. Han, K. D. Lee, N. J. Hur, M. Arita, K. Shimada, H. Namatame, and M. Taniguchi, Phys. Rev. Lett. **108**, 046805 (2012).

[56] B. Kim, C. H. Kim, P. Kim, W. Jung, Y. Kim, Y. Koh, M. Arita, K. Shimada, H. Namatame, M. Taniguchi, J. Yu, and C. Kim, Phys. Rev. B **85**, 195402 (2012).

[57] J.-H. Park, C. H. Kim, J.-W. Rhim, and J. H. Han, Phys. Rev. B **85**, 195401 (2012).

[58] M. Kim, J. Ihm, and S. B. Chung, Phys. Rev. B **94**, 115431 (2016).

[59] W. Lin, L. Li, F. Doşan, C. Li, H. Rotella, X. Yu, B. Zhang, Y. Li, W. S. Lew, S. Wang, W. Prellier, S. J. Pennycook, J. Chen, Z. Zhong, A. Manchon, and T. Wu, Nat. Commun. **10**, 3052 (2019).

[60] W. S. Kyung, S. S. Huh, Y. Y. Koh, K.-Y. Choi, M. Nakajima, H. Eisaki, J. D. Denlinger, S.-K. Mo, C. Kim, and Y. K. Kim, Nat. Mater. **15**, 1233 (2016).